Electronic structures and magnetic properties in $Sr_{1-x}La_xRuO_3$ ($0.0 \leq x \leq 0.5$)

2002 J. Phys.: Condens. Matter 14 415

(http://iopscience.iop.org/0953-8984/14/3/311)

INSTITUTE OF PHYSICS PUBLISHING JOURNAL OF PHYSICS: CONDENSED MATTER

J. Phys.: Condens. Matter **14** (2002) 415–425 PII: S0953-8984(02)29239-5

Electronic structures and magnetic properties in $Sr_{1-x}La_xRuO_3$ ($0.0 \leqslant x \leqslant 0.5$)

H Nakatsugawa[1,3], **E Iguchi**[1] **and Y Oohara**[2]

[1] Division of Materials Science and Engineering, Graduate School of Engineering, Yokohama National University, Tokiwadai, Hodogaya-Ku, Yokohama 240-8501, Japan
[2] Neutron Scattering Laboratory, Institute for Solid State Physics, University of Tokyo, Shirakata 106-1, Tokai 319-1106, Japan

E-mail: hiro@post.me.ynu.ac.jp

Received 28 September 2001, in final form 3 December 2001
Published 21 December 2001
Online at stacks.iop.org/JPhysCM/14/415

Abstract

In order to find out more about the suppression of ferromagnetic (FM) interactions in $Sr_{1-x}La_xRuO_3$, electronic structures and magnetic properties have been investigated upon changing x from 0.0 to 0.5, using an XRD method with Rietveld analysis, a SQUID magnetometer and a DV-Xα computational method. In comparison with magnetic properties in $Sr_{1-x}Ca_xRuO_3$, FM interactions in $Sr_{1-x}La_xRuO_3$ are found to be suppressed very rapidly against x. Neither structural distortion nor cation-size disorder can account for such rapid suppression. Instead, this may be attributed to the effect of La–O hybridization created by La substitution for Sr. This hybridization effect weakens the FM order around Ru ions and, as a result, the long-range FM states are suppressed even if x is small. The DV-Xα cluster method was employed to estimate the energy difference between the up and down spin density of states in $SrRuO_3$ and $Sr_{0.5}La_{0.5}RuO_3$. This calculation predicts that $Sr_{1-x}La_xRuO_3$ contains La–O hybridization which suppresses FM interaction even at small x.

(Some figures in this article are in colour only in the electronic version)

1. Introduction

Because of the spin-triplet p-wave superconductivity in the copper-free layered perovskite Sr_2RuO_4 [1, 2], the anomalous magnetic and transport properties of this material and the related ruthenium oxides have attracted much interest. A series of ruthenium oxides $(Sr, Ca)_{n+1}Ru_nO_{3n+1}$ shows a variety of properties: a ferromagnetic (FM) metal, an antiferromagnetic (AFM) insulator and a superconductor. In particular, a correct understanding

[3] Author to whom any correspondence should be addressed.

of the magnetic properties in these ruthenates is indispensable if we are to gain an insight into the emergence of spin-triplet superconductivity in Sr_2RuO_4.

$SrRuO_3$ and $CaRuO_3$, which are $n = \infty$ members of the series, have nearly cubic and slightly distorted cubic perovskite structure respectively. Though both the ruthenates exhibit metallic behaviour [3, 4], their magnetic properties differ remarkably: $SrRuO_3$ is a FM metal with Curie temperature $T_C = 160$ K [5, 6] whereas $CaRuO_3$ does not show any magnetic anomalies even at very low temperatures. Such a magnetic difference has been mainly ascribed to the ionic sizes of Sr^{2+} (1.44 Å) and Ca^{2+} (1.34 Å), although there must be various reasons. Because the ionic radius of Sr^{2+} is bigger than that of Ca^{2+}, $CaRuO_3$ is more distorted [5]. In $Sr_{1-x}Ca_xRuO_3$, each RuO_6 octahedron is tilted slightly and rotated around Ca^{2+} substituted for Sr^{2+} to fill the extra space of the Sr-shared positions. The calculated band structures also suggest the importance of the structural distortion. In the band structure constructed by Mazin *et al* [7], the density of states (DOS) in $SrRuO_3$ has a strong peak at the Fermi level, stabilizing FM states, while $CaRuO_3$ is on the border of FM states and paramagnetic (PM) states due to the fact that the more distorted structure of $CaRuO_3$ lowers the DOS at the Fermi level [7]. In another calculation by Fukunaga *et al* [8], FM ground states are formed in both compounds, but the energies obtained in the calculations, especially for $CaRuO_3$, are very sensitive to the calculational parameters employed. It has also been argued that the larger structural distortion in $CaRuO_3$ would result in larger splitting of the Ru t_{2g} orbital, leading to stronger AFM interactions [9]. He *et al* have recently concluded that $CaRuO_3$ is not a classical AFM, but is rather poised at a critical point between FM and PM ground states [10, 11].

There are several publications which study the properties of $Sr_{1-x}Ca_xRuO_3$ perovskites [9–15]. The variation in properties due to the change in x is now basically understood in terms of the change in magnetic ground state as a function of the Ru–O–Ru bond angle [7], but there must be other parameters to consider. The size disorder of A-site atoms must be also an important parameter. In a study of the magnetism and the size-disorder effect on the magnetic properties in 4d-based ruthenate perovskites, experiments on $Sr_{1-x}La_xRuO_3$ could provide very useful information. Comparing the ionic radius of La^{3+} (1.36 Å) with the ionic radii of Sr^{2+} and Ca^{2+}, $Sr_{1-x}La_xRuO_3$ is expected to have orthorhombic distortion and the size disorder, both of which are smaller than those of $Sr_{1-x}Ca_xRuO_3$. In order to investigate the effects due to the orthorhombic distortion and the cation-size disorder, elucidation of structural lattice parameters and magnetic properties in $Sr_{1-x}La_xRuO_3$ as a function of x is necessary. Furthermore, there is a high possibility that La^{3+} substituted for Sr^{2+} changes the electronic structure of ions and the nature of the chemical bond. From these points of view, the structural lattice parameters, the magnetic properties and the electronic structures in a series of $Sr_{1-x}La_xRuO_3$ perovskites ($0.0 \leqslant x \leqslant 0.5$) have been investigated in the present study, using the powder x-ray diffraction (XRD) method with Rietveld analysis, a SQUID magnetometer and the discrete variational (DV)-Xα computational method.

2. Experimental details

Polycrystalline samples of $Sr_{1-x}La_xRuO_3$ ($x = 0.0, 0.1, 0.2, 0.3, 0.4$ and 0.5) were synthesized by a conventional solid state reaction method. Stoichiometric mixtures of powders of $SrCO_3$ (99.99%), dried La_2O_3 (99.99%) and dried RuO_2 (99.95%) were ground and reacted at 1373 K for 24 h in air. This procedure was repeated several times. The samples were reground, pressed into pellets, heated again at 1573 K for 24 h in air and cooled to room temperature at a rate of 1 K min^{-1}. All of the sintered pellets were analysed at room temperature, using an x-ray diffractometer with a graphite monochromator and Cu K_α radiation with step scanning. The powder XRD patterns show a single-phase compound with *Pnma* type space

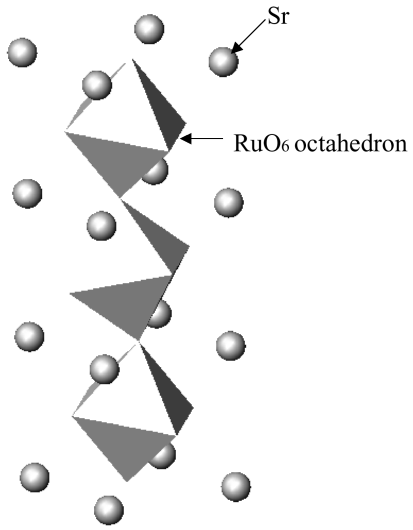

Figure 1. Model cluster used in the DV-Xα cluster method, i.e. an $[Sr_{16}Ru_3O_{16}]^{12+}$ cluster which is employed in the present calculation for $SrRuO_3$ ($x = 0.0$).

symmetry (no 62) for every sample. The structural lattice parameters were refined using a Rietveld analysis program, RIETAN-2000 [16]. The magnetization of $Sr_{1-x}La_xRuO_3$ was measured using a SQUID magnetometer (quantum design MPMS) as a function of temperature ($5\ K \leqslant T \leqslant 300\ K$) at 100 Oe on field cooling.

3. Computational procedures

Interpretation of the experimental results obtained here requires the assistance of theoretical calculations. All computations were performed by means of an *ab initio* molecular orbital (MO) method using model clusters. The computer code called SCAT [17], which is a modified version of the original DV-Xα program [18,19], was employed. Slater's exchange and correlation term with $\alpha = 0.7$ was used, and spin polarizations were taken into account in the calculations [20]. Numerical atomic orbitals (NAOs) were used as basis functions. They were generated flexibly by solving the radial part of the Schrödinger equation for a given environment. Basis sets were 1s–5s for Sr, 1s–6p for La, 1s–5p for Ru and 1s–2p for O. Integrations to obtain energy eigenvalues and eigenfunctions were made numerically. Population analyses were made in the standard Mulliken manner [21]. Calculations of the electronic structures have been carried out under the assumption that the electronic structures of $[Sr_{16}Ru_3O_{16}]^{12+}$ and $[Sr_8La_8Ru_3O_{16}]^{18.5+}$ clusters are representative of those of $SrRuO_3$ ($x = 0.0$) and $Sr_{0.5}La_{0.5}RuO_3$ ($x = 0.5$) respectively. Figure 1 shows the structure of the $[Sr_{16}Ru_3O_{16}]^{12+}$ cluster employed in the present calculation for $x = 0.0$. The model clusters were embedded in a Madelung potential generated by approximately 10 000 point charges of formal values. The values were +2, +4 and −2 for Sr, Ru and O in $SrRuO_3$. In $Sr_{0.5}La_{0.5}RuO_3$, they were +2, +3, +3.5 and −2 for Sr, La, Ru and O. Convergence of the electrostatic potential with respect to dipole and quadrupole sums [22] was established within an accuracy of 0.1%.

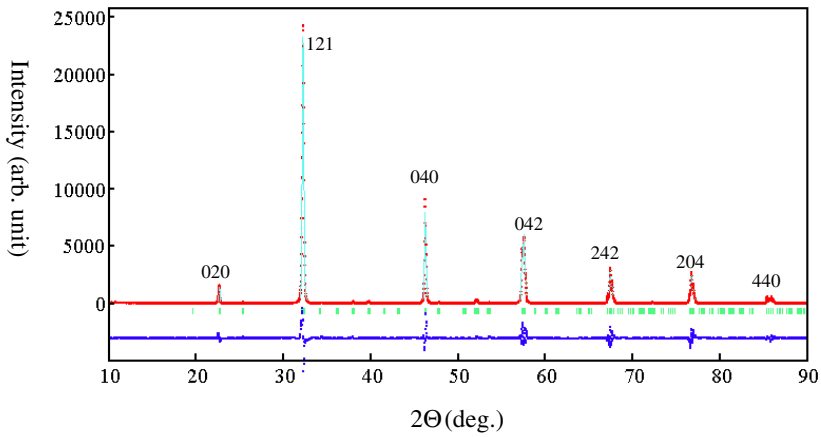

Figure 2. Observed (dotted curve) and calculated (full curve) intensities in powder XRD of $SrRuO_3$ ($x = 0.0$). Tick marks represent the positions of possible Bragg reflections. The full curve at the bottom is the difference between observed and calculated intensities.

4. Results and discussion

4.1. Crystal structures

No impurity peak was detected in the present powder XRD measurements, and all samples of $Sr_{1-x}La_xRuO_3$ had the $GdFeO_3$ type orthorhombic perovskite structure. Figure 2 shows observed, calculated and difference intensities in the XRD pattern of $SrRuO_3$ ($x = 0.0$). Detailed results of the structural refinements are presented in table 1. The cubic subcell parameters of $Sr_{1-x}La_xRuO_3$ are shown in figure 3(a). All three lattice constants, a, b and c, increase with increasing x, although Sr^{2+} (1.44 Å) is replaced with La^{3+} (1.36 Å). There is, however, an anomaly around $x \cong 0.3$ in the lattice constant b. This must be because electronic structures and magnetic properties change at $x \cong 0.3$. Furthermore, the Ru–O(1)–Ru and Ru–O(2)–Ru bond angles also cross at $x \cong 0.3$, as shown in figure 3(b). The decrease in the Ru–O(1)–Ru bond angle with increasing x suggests the rotation of RuO_6 octahedra around La^{3+} substituted for Sr^{2+} in the similar way to $Sr_{1-x}Ca_xRuO_3$ due to the ionic radius of La^{3+} being smaller than that of Sr^{2+}. Table 2 shows the Ru–O(1)–Ru and Ru–O(2)–Ru bond angles, the Ru–O(1) and Ru–O(2) bond lengths and the ionic spaces between the A-site ion and the O ion, i.e. $Sr_{1-x}La_x$–O(1) and $Sr_{1-x}La_x$–O(2), for every sample. Look at the average Ru–O bond length in table 2; one finds a monotonic increase in bond length with increasing x. This must be because the variation of x changes the Ru oxidation state. Thus, the Ru–O–Ru bond angle between RuO_6 octahedra and the Ru–O bond lengths within RuO_6 octahedra change as x increases.

4.2. Magnetic properties

The series of $Sr_{1-x}La_xRuO_3$ exhibits complicated magnetic properties. Figure 4 demonstrates temperature dependences of the magnetic susceptibilities χ measured at 100 Oe on field cooling as a parametric function of x. The ferromagnetism is very greatly attenuated with increasing x. Figure 5 plots the inverse magnetic susceptibility $1/\chi$ against T for each specimen. The Curie–Weiss relation, $\chi = \chi_0 + C/(T - \Theta)$, holds at each x in the temperature range $T > \sim 160$ K except for $x = 0.5$, where χ_0 is estimated to a precision of $\pm 10^{-5}$ emu mol^{-1} Ru, the Curie constant C is determined by a least squares method, and Θ is the Curie–Weiss temperature.

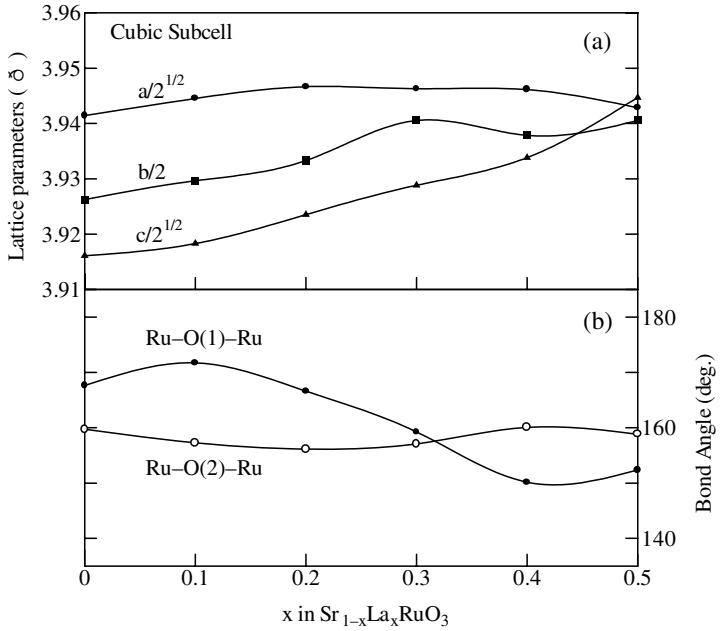

Figure 3. Selected structural data for $Sr_{1-x}La_xRuO_3$ ($0.0 \leqslant x \leqslant 0.5$). (a) the cubic subcell parameters of $Sr_{1-x}La_xRuO_3$ and (b) the Ru–O(1)–Ru and Ru–O(2)–Ru bond angle. Curves are guides to the eye.

Table 1. Structural parameters for $Sr_{1-x}La_xRuO_3$ ($0.0 \leqslant x \leqslant 0.5$) at room temperature. Space group: *Pnma* (no 62). Atomic positions: $Sr_{1-x}La_x$: $4c(x, 1/4, z)$; Ru: $4b(0, 0, 0)$; O(1): $4c(x, 1/4, z)$; O(2): $8d(x, y, z)$.

		$x = 0.0$	$x = 0.1$	$x = 0.2$	$x = 0.3$	$x = 0.4$	$x = 0.5$
$Sr_{1-x}La_x$	x	0.488(3)	0.485(4)	0.483(8)	0.480(9)	0.477(0)	0.470(3)
	z	1.00(0)	1.00(2)	1.00(1)	1.00(0)	0.99(8)	0.996(6)
O(1)	x	−0.000(1)	−0.000(9)	0.000(3)	0.000(1)	0.007(8)	0.004(8)
	z	0.03(8)	0.02(5)	0.04(1)	0.06(4)	0.09(3)	0.08(6)
O(2)	x	0.28(5)	0.28(6)	0.29(4)	0.28(5)	0.28(7)	0.28(5)
	y	−0.03(3)	−0.03(9)	−0.03(8)	−0.04(0)	−0.02(7)	−0.03(0)
	z	0.22(7)	0.22(3)	0.22(1)	0.22(4)	0.21(9)	0.21(5)
Lattice	a (Å)	5.574(0)	5.578(4)	5.581(4)	5.580(9)	5.580(6)	5.576(0)
parameters	b (Å)	7.852(5)	7.859(3)	7.866(6)	7.881(1)	7.875(7)	7.881(0)
	c (Å)	5.538(2)	5.541(3)	5.548(7)	5.556(2)	5.563(2)	5.578(6)
	V (Å^3)	242.4(1)	242.9(4)	243.6(2)	244.3(8)	244.5(2)	245.1(6)
R-factors	$R_{wp}(\%)$	16.84	12.82	13.92	17.69	14.39	13.00
	$R_I(\%)$	3.02	2.12	2.91	4.36	2.85	2.27
	R_{wp}/R_e	2.42	1.71	1.87	2.22	1.77	1.58

Figure 6 plots the effective magnetic moment μ_{eff} and Θ as a function of x, where μ_{eff} is calculated using the experimental value for C, i.e. $\mu_{\text{eff}} \cong \sqrt{8C}\mu_B$.

In the μ_{eff} and x relation there is also an anomaly around $x \cong 0.3$, as shown in figure 6. This is the quite similar to the anomalies occurring in the lattice constant b and the Ru–O–Ru bond angle at $x \cong 0.3$. The Curie–Weiss temperature also decreases smoothly with increasing

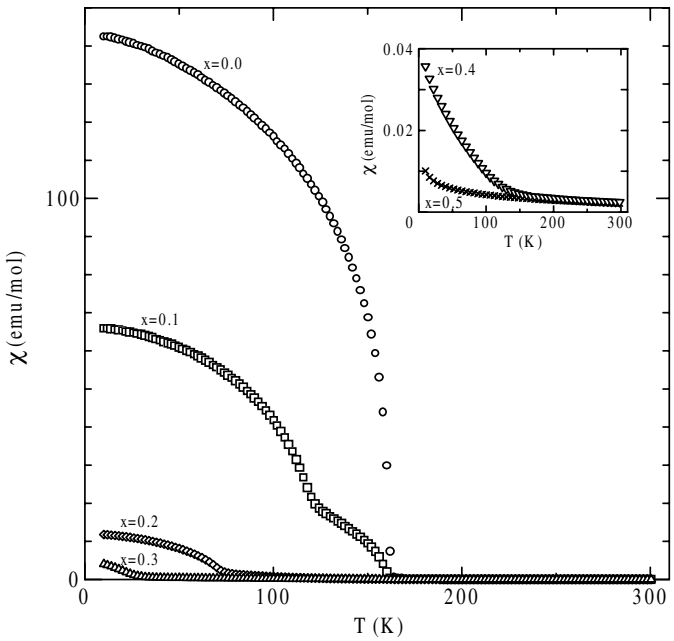

Figure 4. Temperature dependence of the magnetic susceptibility measured at 100 Oe on field cooling for $Sr_{1-x}La_xRuO_3$ ($0.0 \leqslant x \leqslant 0.3$). The inset shows the temperature dependence of χ for $x = 0.4$ and 0.5.

Table 2. Selected interatomic distances (Å) and bond angles (deg) for $Sr_{1-x}La_xRuO_3$ ($0.0 \leqslant x \leqslant 0.5$) at room temperature.

		$x = 0.0$	$x = 0.1$	$x = 0.2$	$x = 0.3$	$x = 0.4$	$x = 0.5$
$Sr_{1-x}La_x$– O(1)	×1	2.552(5)	2.615(9)	2.537(1)	2.420(0)	2.273(3)	2.333(0)
$Sr_{1-x}La_x$– O(1)	×1	2.730(5)	2.716(2)	2.707(3)	2.707(5)	2.671(8)	2.643(8)
$Sr_{1-x}La_x$– O(1)	×1	2.858(9)	2.868(1)	2.891(7)	2.919(8)	3.009(1)	3.022(4)
$Sr_{1-x}La_x$– O(1)	×1	2.987(2)	2.927(5)	3.014(7)	3.140(4)	3.300(9)	3.259(3)
$Sr_{1-x}La_x$– O(2)	×2	2.462(7)	2.436(1)	2.416(8)	2.446(1)	2.502(3)	2.496(5)
$Sr_{1-x}La_x$– O(2)	×2	2.740(9)	2.727(6)	2.756(5)	2.700(1)	2.724(4)	2.730(4)
$Sr_{1-x}La_x$– O(2)	×2	2.795(3)	2.809(5)	2.783(8)	2.824(3)	2.765(3)	2.734(3)
$Sr_{1-x}La_x$– O(2)	×2	3.159(1)	3.207(4)	3.241(1)	3.235(7)	3.201(1)	3.251(3)
Ru–O(1)	×2	1.974(6)	1.969(9)	1.980(1)	2.003(0)	2.037(5)	2.028(8)
Ru–O(2)	×2	1.944(4)	1.965(4)	1.950(4)	1.967(1)	1.973(6)	1.999(7)
Ru–O(2)	×2	2.046(6)	2.044(6)	2.071(4)	2.050(5)	2.026(6)	2.012(3)
Avg. Ru–O		1.988	1.993	2.000	2.006	2.012	2.013
Ru–O(1)–Ru		167.6(4)	171.7(4)	166.6(2)	159.2(7)	150.1(7)	152.3(9)
Ru–O(2)–Ru		159.7(3)	157.2(8)	156.1(4)	157.0(9)	160.0(7)	158.8(3)

x as well for $Sr_{1-x}Ca_xRuO_3$ [4]. It is noteworthy, however, that Θ changes from positive to negative at $x \cong 0.3$ in $Sr_{1-x}La_xRuO_3$ but at $x \cong 0.9$ in $Sr_{1-x}Ca_xRuO_3$ [4]. If the structural distortion were the predominant reason for suppression of FM states, Θ in $Sr_{1-x}Ca_xRuO_3$ would be lower than that in $Sr_{1-x}La_xRuO_3$ at the same doping level. However, the reverse is shownin the experiments. There must therefore be some reason other than the lattice distortion responsible for such magnetic behaviours.

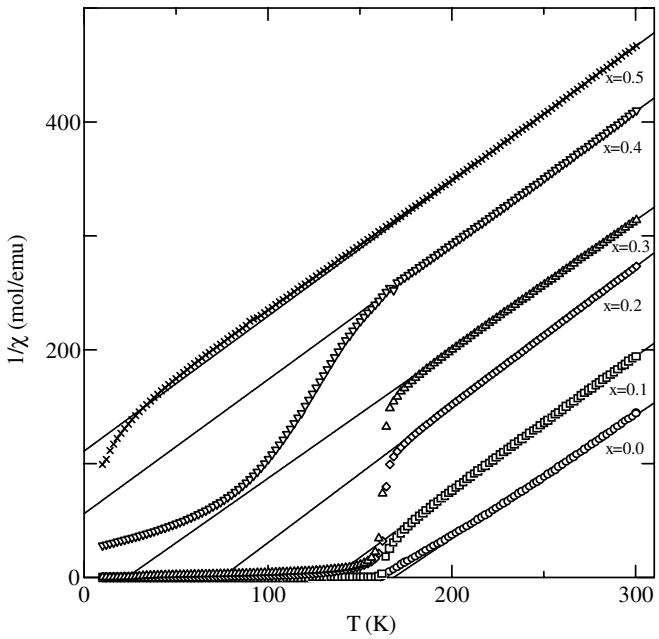

Figure 5. Temperature dependence of the inverse magnetic susceptibility measured at 100 Oe on field cooling for $Sr_{1-x}La_xRuO_3$ ($0.0 \leqslant x \leqslant 0.5$).

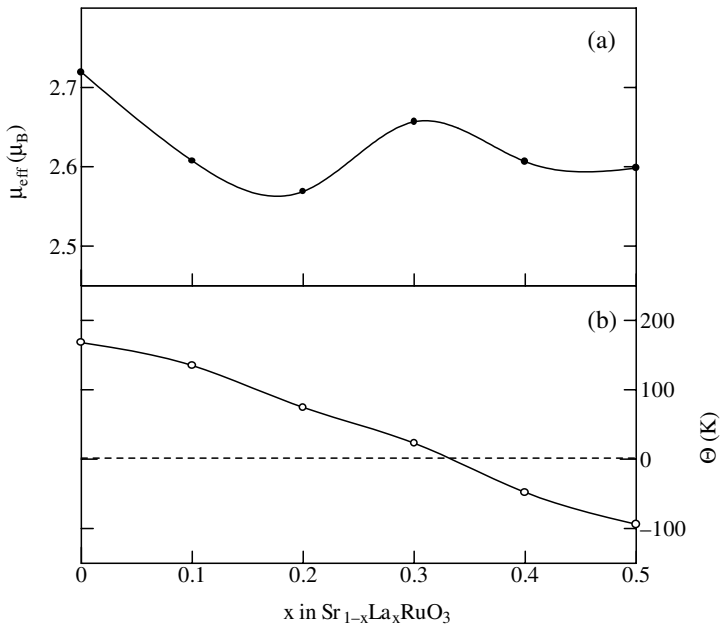

Figure 6. Component dependence of (a) the effective magnetic moment and (b) Curie–Weiss temperatures for $Sr_{1-x}La_xRuO_3$ ($0.0 \leqslant x \leqslant 0.5$), derived from the data in figure 5. Curves are guides to the eye.

In order to understand correctly the relationship between Θ and the structural distortions in the 4d-based ruthenate perovskites, calculations of the magnetic exchange interactions in t_{2g} compounds are very helpful because Θ is very sensitively dependent on the magnetic exchange interactions. Experimental and theoretical studies on the 3d perovskites with unpaired electrons in the e_g orbital are indicative of the transition from AFM to FM by the magnetic exchange interactions as the M e_g–O 2p–M e_g bond angle decreases from 180° to 90°, where M is a 3d transition metal [23, 24]. In $Sr_{1-x}La_xRuO_3$, the interacting orbital is Ru t_{2g}–O 2p–Ru t_{2g}. In this case, the situation becomes more complicated. As the Ru–O–Ru bond angle decreases, the 180° π-type p–d interaction decreases, but the σ-type-like p–d interaction becomes strong [10]. Furthermore, the two t_{2g} orbitals in bond through the O ion can interact directly. Since $Sr_{1-x}La_xRuO_3$ contains these interactions, detailed calculations on the electronic structures in this system are necessary in order to explain the magnetic properties and the variation of lattice parameters obtained in the present study. The DV-Xα cluster method was employed as the computing method [17–22].

4.3. Electronic structures

The average net charges evaluated for $[Sr_{16}Ru_3O_{16}]^{12+}$ and $[Sr_8La_8Ru_3O_{16}]^{18.5+}$ clusters at $x = 0.0$ and 0.5 are $+2.28e$ and $+1.98e$ for Ru, $+1.95e$ and $+1.97e$ for Sr, and $-1.63e$ and $-1.43e$ for O. There must be a small covalent component in the bonding between a cation and an anion. Total DOS and partial DOS of $SrRuO_3$ ($x = 0.0$) and $Sr_{0.5}La_{0.5}RuO_3$ ($x = 0.5$) are illustrated in figure 7 together with energy level diagrams. All of the theoretical curves in figure 7 are the results computed by broadening discrete MO energy eigenvalues, using a Gaussian function of 0.5 eV full width at half maximum (FWHM) for easy visualization of the DOS. As shown in figure 7(a), the filled band located from −10 to 0 eV is mainly composed of Ru 4d and O 2p orbital at $x = 0.0$. This indicates that the electronic structure around the Fermi level consists of Ru 4d and O 2p orbitals which are hybridized. Figure 7(b) demonstrates the energy levels at $x = 0.5$ together with the energy difference between up and down spin in the Ru 4d partial DOS. The electronic structure around the Fermi level consists of Ru 4d, La 4f, O 2p orbitals which are also hybridized.

In the theory behind the Curie–Weiss law, the positive Θ indicates FM interactions between spins and the negative Θ indicates AFM. In this scenario, FM and AFM interactions coexist within $Sr_{1-x}La_xRuO_3$, and the ratio of FM to AFM interaction changes with the variation of x. The heavy Ru–O hybridization is included in $SrRuO_3$ (see figure 7(a)). The magnetic result in figure 4 indicates that this hybridization stabilizes the FM ground state because of the maximum susceptibility at $x = 0.0$. As the amount of La increases, the Ru–O hybridization is attenuated gradually and instead the La–O hybridization emerges above the Fermi level. The attenuation of Ru–O hybridization is likely to destabilize FM states. As a result, the Ru t_{2g}–O 2p–Ru t_{2g} type superexchange interaction is expected to be predominantly AFM states at a large x. This speculation is consistent with the decrease in Θ as shown in figure 6(b). Then the smooth decrease on Θ in $Sr_{1-x}La_xRuO_3$ with increasing x means a change in the relative strength of FM and AFM interactions. Though the AFM interactions are competitive with the FM interactions around $x \cong 0.3$, AFM becomes superior to FM when x increases further. This means that the La–O hybridization increases and the Ru–O hybridization is somewhat attenuated above $x \cong 0.3$. The Ru–O(1) bond length contributes most directly to the variation of the lattice constant b, because the Ru–O(1) bond length generally increases through $x \cong 0.3$ as shown in table 2, implying the attenuation of Ru–O(1) hybridization. Though the tilt and rotation of RuO_6 octahedra and the average ionic size at the A-site cause the lattice constants to vary more significantly than the nature of the bond, the increase in the Ru–O(1) bond length

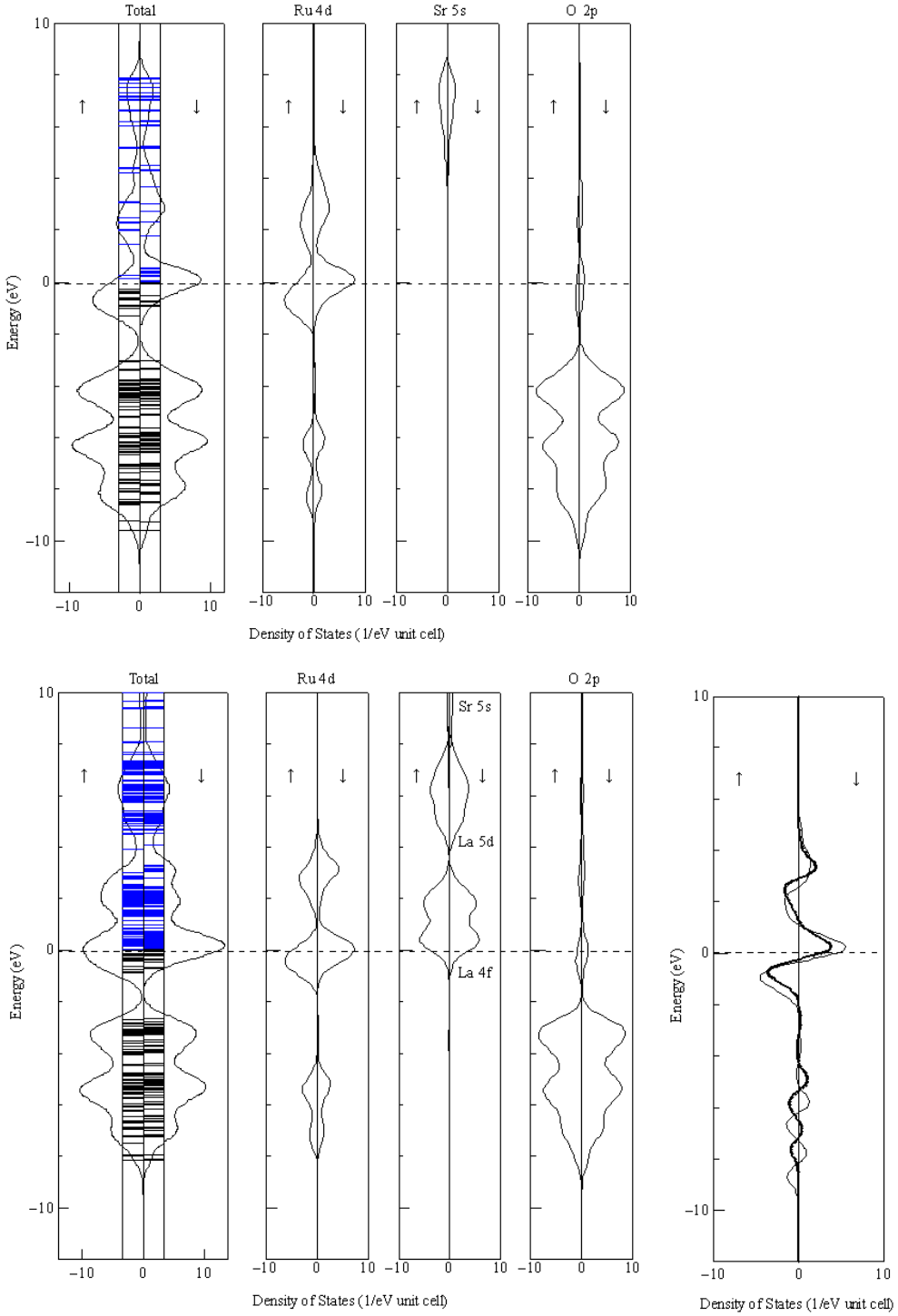

Figure 7. Energy level diagrams and total and partial DOS of (top) $SrRuO_3$ ($x = 0.0$) for the $[Sr_{16}Ru_3O_{16}]^{12+}$ cluster and (bottom) $Sr_{0.5}La_{0.5}RuO_3$ ($x = 0.5$) for the $[Sr_8La_8Ru_3O_{16}]^{18.5+}$ cluster together with the energy difference between up and down spin DOS, where solid and broken curves indicate that of $SrRuO_3$ ($x = 0.0$) and $Sr_{0.5}La_{0.5}RuO_3$ ($x = 0.5$) respectively.

must be one of the main reasons for the anomaly in the lattice constant b around $x \cong 0.3$. Though the attenuation of the Ru–O(1) hybridization may have some effects on the increase in μ_{eff} around $x \cong 0.3$ as shown in figure 6(a), the AFM effects must suppress this increase in μ_{eff} at $x > 0.3$ as illustrated in figure 6(b).

There is an energy difference between up and down spin in Ru 4d partial DOS. This difference forms FM states. As shown in figure 7(b), the energy difference between up and down spin in Ru 4d partial DOS in $SrRuO_3$ ($x = 0.0$) is larger than that in $Sr_{0.5}La_{0.5}RuO_3$ ($x = 0.5$). This means that FM states are suppressed with increasing x. The unoccupied DOS located above the Fermi level is mainly made up of Ru–O and Sr–O hybridization, even though La–O hybridization is included at $x = 0.5$ as shown in figure 7(b). The La–O hybridization above the Fermi level affects the local magnetic environment around Ru and the local charge state of Ru. Moreover, the local electron densities throughout the Ru–O network are likely to fluctuate due to the La–O hybridization. Such a fluctuation weakens somewhat the Ru–O hybridization and also the FM interaction between Ru 4d spins. As a result, FM states in $Sr_{1-x}La_xRuO_3$ are suppressed.

5. Conclusion

The structural lattice parameters, the magnetic properties and the electronic structures in $Sr_{1-x}La_xRuO_3$ have been investigated using the XRD method with a Rietveld analysis, a SQUID magnetometer and the DV-Xα computational method. Variation of x changes the Ru oxidation so that the Ru–O–Ru bond angle between RuO_6 octahedra and the Ru–O bond lengths within RuO_6 octahedra change as x increases. The ferromagnetism is suppressed very remarkably with increasing x. It is noteworthy that Θ changes from positive to negative at $x \cong 0.3$ in $Sr_{1-x}La_xRuO_3$ but at $x \cong 0.9$ in $Sr_{1-x}Ca_xRuO_3$. If the structural distortion were the predominant factor in suppressing FM states, Θ in $Sr_{1-x}Ca_xRuO_3$ would be lower than that in $Sr_{1-x}La_xRuO_3$ at the same doping level. However, the reverse is found in the experiments. There must therefore be some reason for such magnetic behaviour in addition to the lattice distortion due to the difference in the ionic sizes of Ca^{2+} and La^{3+}. Since $Sr_{1-x}La_xRuO_3$ contains Ru t_{2g}–O 2p–Ru t_{2g} interactions, detailed calculations of the electronic structures in this system are necessary in order to explain the magnetic properties and the variation of lattice parameters. The energy difference between up and down spin in Ru 4d partial DOS in $SrRuO_3$ is larger than that in $Sr_{0.5}La_{0.5}RuO_3$. This means that FM states are suppressed with increasing x. In addition, the La–O hybridization above the Fermi level affects the local magnetic environment around Ru and the local charge state of Ru. The local electron densities throughout the Ru–O network are likely to fluctuate due to the La–O hybridization. Such a fluctuation weakens somewhat the Ru–O hybridization and also the FM interaction between Ru 4d spins. As a result, FM states in $Sr_{1-x}La_xRuO_3$ are suppressed.

Acknowledgments

This work was supported by Ogasawara foundation for the promotion of science and engineering and Arai foundation for the promotion of science and engineering. The SQUID magnetometer in the Ecotechnology System Laboratory, Yokohama National University, was used.

References

[1] Maeno Y, Hashimoto H, Yoshida K, Nishizaki S, Fujita T, Bednorz J B and Lichtenberg F 1994 *Nature* **372** 532
[2] Ishida K, Mukuda H, Kitaoka Y, Asayama K, Mao Z Q, Mori Y and Maeno Y 1998 *Nature* **396** 658

[3] Kobayashi H, Nagata M, Kanno R and Kawamoto Y 1994 *Mater. Res. Bull.* **29** 1271
[4] Gao G, McCall S, Shepard M, Crow J E and Guertin R P 1997 *Phys. Rev.* B **56** 321
[5] Callaghan A, Moeller C W and Ward R 1966 *Inorg. Chem.* **5** 1572
[6] Longo J M, Raccah P M and Goodenough J B 1968 *J. Appl. Phys.* **39** 1327
[7] Mazin I and Singh D J 1997 *Phys. Rev.* B **56** 2556
[8] Santi G and Jarlborg T 1997 *J. Phys.: Condens. Matter* **9** 9563
[9] Fukunaga F and Tsuda N 1994 *J. Phys. Soc. Japan* **63** 3798
[10] He T, Huang Q and Cava R J 2001 *Phys. Rev.* B **63** 024402
[11] He T and Cava R J 2001 *J. Phys.: Condens. Matter* **13** 8347
[12] Yoshimura K, Imai T, Kiyama T, Thurber K R, Hunt A W and Kosuge K 1999 *Phys. Rev. Lett.* **83** 4397
[13] Kiyama T, Yoshimura K, Kosuge K, Michor H and Hilscher G 1998 *J. Phys. Soc. Japan* **67** 307
[14] Kiyama T, Yoshimura K and Kosuge K 1999 *J. Phys. Soc. Japan* **68** 3372
[15] Mukuda H, Ishida K, Kitaoka Y, Asayama K, Kanno R and Takano M 1999 *Phys. Rev.* B **60** 12 279
[16] Izumi F 1993 *The Rietveld Method* ed R A Young (Oxford: Oxford University Press) ch 13
[17] Adachi H, Tsukada M and Satoko C 1978 *J. Phys. Soc. Japan* **45** 875
[18] Averill F W and Ellis D E 1973 *J. Chem. Phys.* **59** 6412
[19] Ellis D E, Adachi H and Averill F W 1976 *Surf. Sci.* **58** 497
[20] Nakatsugawa H and Iguchi E 2000 *Japan. J. Appl. Phys.* **39** 1186
[21] Mulliken R S 1955 *J. Chem. Phys.* **23** 1833
[22] Coker H 1983 *J. Phys. C: Solid State Phys.* **87** 2512
[23] García-Muñoz J L, Fontcuberta J, Suaaidi M and Obradors X 1996 *J. Phys.: Condens. Matter* **8** L787
[24] Asai K, Fujiyoshi K, Nishimori N, Satoh Y, Kobayashi Y and Mizoguchi M 1998 *J. Phys. Soc. Japan* **67** 4218